The Astrophysical Journal, 904:31 (12pp), 2020 November 20 https://doi.org/10.3847/1538-4357/abbacb

Statistical and Observational Research on Solar Flare EUV Spectra and Geometrical Features

Shohei Nishimoto[1], Kyoko Watanabe[1], Shinsuke Imada[2], Tomoko Kawate[3], and Kyoung-Sun Lee[4]
[1] National Defense Academy of Japan, 1-10-20 Hashirimizu, Yokosuka, Kanagawa 239-8686, Japan
[2] Institute for Space-Earth Environmental Research (ISEE), Nagoya University, Furo-cho, Chikusa-ku, Nagoya, Aichi 464-8601, Japan
[3] National Institute for Fusion Science, 322-6 Oroshi-cho, Toki, Gifu 509-5292, Japan
[4] Center for Space Plasma and Aeronomic Research, University of Alabama in Huntsville, 320 Sparkman Drive, Huntsville, AL 35805, USA
Received 2020 March 4; revised 2020 September 12; accepted 2020 September 19; published 2020 November 19

Abstract

We performed statistical analysis on the flare emission data to examine parameters related to the flare extreme-ultraviolet (EUV) spectra. This study used the data from the Geostationary Operational Environmental Satellite X-ray Sensors to determine the fundamental flare parameters. The relationship between soft X-ray data and EUV emission data observed by the Extreme Ultraviolet Variability Experiment on board the Solar Dynamics Observatory (SDO) MEGS-A was investigated for 50 events. The results showed the hotter Fe line emissions have strong correlation with soft X-ray data in many cases. However, our statistical study revealed that EUV flare peak flux of Fe XV, Fe XVI and He II lines have weak correlation with soft X-ray peak flux. In EUV line light curves, there was time difference in peak time, however the tendency to reach the peak in order from the hotter line to cooler line was not so clear. These results indicate that the temporal evolution of EUV emission can be roughly explained by soft X-ray data. However, the time changes of temperature and density distributions in the flare loop must be needed for accurate reproduction. Moreover, we compared the geometrical features of solar flares observed by the Atmospheric Imaging Assembly on board the SDO with the fundamental flare parameters for 32 events. The ribbon distance strongly correlated with both soft X-ray flare rise and decay times. This results indicate that the geometrical feature is essential parameter for predicting flare emission duration.

Unified Astronomy Thesaurus concepts: Solar flares (1496); Solar flare spectra (1982)

1. Introduction

In recent years, the demand for space utilization has increased; hence, it is very important to accurately grasp the status of the solar-terrestrial environment, which is strongly influenced by solar activities. Among many solar activities, solar flares have a significant impact on space weather. When X-ray and/or extreme-ultraviolet (EUV) emissions from solar flares reach the Earth's atmosphere, they are absorbed by the thermosphere and ionosphere. The X-ray and shorter wavelength EUV emissions affect the ionosphere D layer, E layer and lower thermosphere. This causes the Sudden Ionospheric Disturbance (Dellinger 1937) and communication failure due to changes in the refractive index of the ionosphere (Thiemann et al. 2019). The longer wavelength EUV emissions dominate ionization in the ionosphere F layer and upper thermosphere (Qian et al. 2011). Due to these EUV emissions, the thermosphere expands and reaches the low earth orbit, causing satellite resistance (Jachhia 1990; Thiemann et al. 2019). The ionosphere response to these solar flare emissions is immediate after flare, and the thermosphere response is after 2–4 hr (Qian et al. 2010). Since there is a very short span of time between the occurrence of the solar flare and space weather impacts, it is difficult to prepare for the disturbances after flare occurrences. Moreover, the space weather impacts occurrence may not correspond to flare class determined by observed flare soft X-ray flux classified by the Geostationary Operational Environmental Satellite (GOES). Due to the lack of correspondence mentioned above, the flare class cannot be considered an optimal index for determining the space weather impacts occurrence. Therefore, it is necessary to investigate the details of the flare emission spectra in solar flares in order to find out which flare emission mainly affects the space weather impacts.

Among these flare emissions, soft X-ray flux have been observed by the GOES satellite continuously since 1975. On the other hands, observational EUV emission data are limited only to the period in which an observational device is in operation. The solar EUV irradiance observations in recent years have been performed by the Solar EUV Monitor (SEM), the Solar EUV Experiment (SEE), and the Extreme Ultraviolet Variability Experiment (EVE) on board the Solar and Heliospheric Observatory (SOHO; Judge et al. 1998), the Thermosphere Ionosphere Mesosphere Energetics and Dynamics (TIMED; Woods et al. 2005), and the Solar Dynamics Observatory (SDO; Woods et al. 2012), respectively. The SOHO/SEM has continuously been observing the solar irradiance at 260–340 Å band and 1–500 Å band at 15 s time cadence since 1996 January. However, the two broad-wavelength band spectral resolution of the SOHO/SEM data is insufficient for study of the variation of each EUV line of the solar flare spectra. The TIMED/SEE has continuously been observing solar irradiance at 1–1940 Å at 4 Å spectral resolution since 2002 January. Although TIMED/SEE exhibits a better spectral resolution than SOHO/SEM, it mainly performs daily observation; hence, it is insufficient for studying short timescale phenomena such as solar flares. The SDO/EVE is the latest instrument, which began observing the full disk solar irradiance in the 1–1060 Å range at a 1 Å spectral resolution and 10 s cadence from 2010 May. The SDO/EVE is of sufficient resolution to study the time variation of EUV spectral lines; however, the SDO/EVE MEGS-A device (which was observing in the 50–370 Å range) was damaged in 2014 May due to CCD power supply malfunction. Although there is much observational EUV emission data available, none covers high spectral and temporal resolution, and no instrument is yet available to provide such kind of data at all times.

Some researchers constructed models to estimate solar flare spectra (e.g., SSPRING, Suess et al. 2016; FISM, Chamberlin et al. 2007, 2008). Currently, the most widely used model for flare emission is the Flare Irradiance Spectral Model (FISM). The FISM can estimate solar irradiance in 1 up to a 1900 Å range at 10 Å resolution and 60 s time cadence. However, the FISM presents two problems. One problem is low prediction accuracy at short wavelength (<140 Å) emissions, which strongly influence to the Earth's lower ionosphere (Woods et al. 2011). Because FISM assumes that the time evolution of EUV emission is proportional to the soft X-ray emission obtained by GOES, it cannot differentiate the time evolution of typical EUV lines that correspond to different temperature plasmas. To accurately determine the time evolutions of flare plasma density and temperature, the physical processes in a solar flare must be taken into consideration (Klimchuk et al. 2008; Cargill et al. 2012).

Currently, the most common physical model for solar flares is the CSHKP model (Carmichael 1964; Sturrock 1966; Hirayama 1974; Kopp & Pneuman 1976; Yokoyama & Shibata 1998; Shiota et al. 2005). Solar flares are thought to be caused by "magnetic reconnection" generated in the corona, which is well confirmed by several observations (Innes & McKenzie 2003; Imada et al. 2013; Warren et al. 2018). Generally, the spatial and temporal scales of a solar flares are 10,000–100,000 km, and about several minutes to several hours, respectively. The energy released by one flare is 10^{29}–10^{32} erg. Magnetic field lines are generated by the Lorentz force between the magnetic field component formed by magnetic reconnection and the current sheet. Strong magnetic tension is generated, and the electrons and protons constituting the corona are heated and accelerated at the same time. The accelerated high-energy particles travel upward and downward along the magnetic field lines. The particles traveling downward fall into the chromosphere, and rapidly heat the surrounding high-density plasma. Then, the high-temperature and high-density plasma rises from the chromosphere along the magnetic field lines in a loop; this is a well-observed phenomenon called chromospheric evaporation (Milligan & Dennis 2009; Imada et al. 2015; Lee et al. 2017). The loop structure of soft X-ray and EUV formed from chromospheric evaporation is called "flare loop," while the two feet of the flare loop are called "foot points." The bright ultraviolet (UV) emission at the bottom of the flare loops is called "flare ribbon." When the accelerated high-energy particles reach the foot-point, spiky EUV emission from the low formation temperature emission lines in the transition layer and chromosphere is observed. Flare loop filled with high-temperature and high-density plasma is cooled conductively and radiatively (Serio et al. 1991; Cargill et al. 1995). Due to conductive loss near the foot-point, transition layer and chromosphere lines are emitted, and in accordance with radiative cooling, EUV lines with higher formation temperature are emitted in the order of lower lines (Hudson 2011; Woods et al. 2011; Thiemann et al. 2017).

The temporal evolution of flare emissions is divided into impulsive and gradual phases (Donnelly 1976; Hudson 2011; Woods et al. 2011). Furthermore, the time evolution of solar flare emission can be divided into the onset phase that enhances the hard X-rays and soft X-ray before the impulsive phase, the extended phase of the second peak of hard X-ray and the gradual phase (Hudson 2011), and the EUV late phase of the second peak on the EUV line (e.g., Fe XVI 33.5 nm) several minutes to hours after the gradual phase (Woods et al. 2011). In this study, we focus on the impulsive and gradual phases composed of soft X-ray and EUV, which account for most of the flare energy and have a large influence on the Earth's thermosphere and ionosphere. The impulsive phase is characterized by a spiky peak at the beginning of the flare, and the gradual phase is indicated by a gentle decrease in intensity (Kane 1974). Radio and hard X-ray emissions show sharp temporal changes of brightness in the impulsive phase, while soft X-ray emission exhibits a slower increase during the impulsive phase, and also shows a gradual decrease during the gradual phase. The EUV emissions comprise both impulsive and gradual components. The impulsive phase originates from the nonthermal emission near the foot-point and the loop-top, while the gradual phase comes from the thermal emission of the flare loop (Hudson 2011).

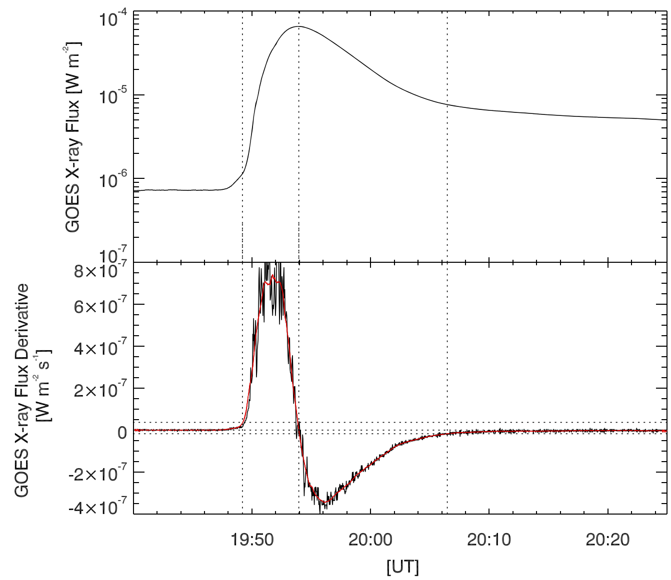

Figure 1. Upper panel: light curve of soft X-ray flux (1–8 Å) by GOES/XRS of the M6.3-class flare on 2013 November 1. Lower panel: light curve of the soft X-ray flux time derivative (black solid line) and 30 s running average of the soft X-ray flux time derivative (red solid line). The vertical dotted lines indicate that flare start time (19:49 UT), peak time (19:54 UT), and end time (20:06 UT), respectively, from the left. The horizontal dotted lines indicate 5% of the flare flux derivative peak, zero for the flare flux derivative, and 5% of the flare flux derivative minus peak, respectively, from the top.

From the above, it is considered that the emission spectra are different between the impulsive phase and the gradual phase because their origins are different. Moreover, it has already been statistically demonstrated that the flare ribbon area is closely related to the flare duration (Toriumi et al. 2017). Since the flare ribbon area reflects the geometric structure such as the flare loop length and depth, in order to accurately understand the flare emission spectra, it is necessary to consider the geometrical structure of flare and the temporal variation of plasma distribution in the flare loop. This consideration will naturally include differences in spectra between the impulsive and gradual phases.

In this study, a statistical analysis was performed on observational flare EUV radiation and geometrical structure to derive parameters effective for flare spectra. The results can help develop a more accurate solar flare emission spectra prediction model based on the physical process associated with the flares.

2. Flare Observation with GOES/XRS, SDO/EVE, and AIA

2.1. Fundamental Parameters from GOES/XRS

We decided to use GOES soft X-ray data as fundamental parameters to compare with flare EUV data and geometrical

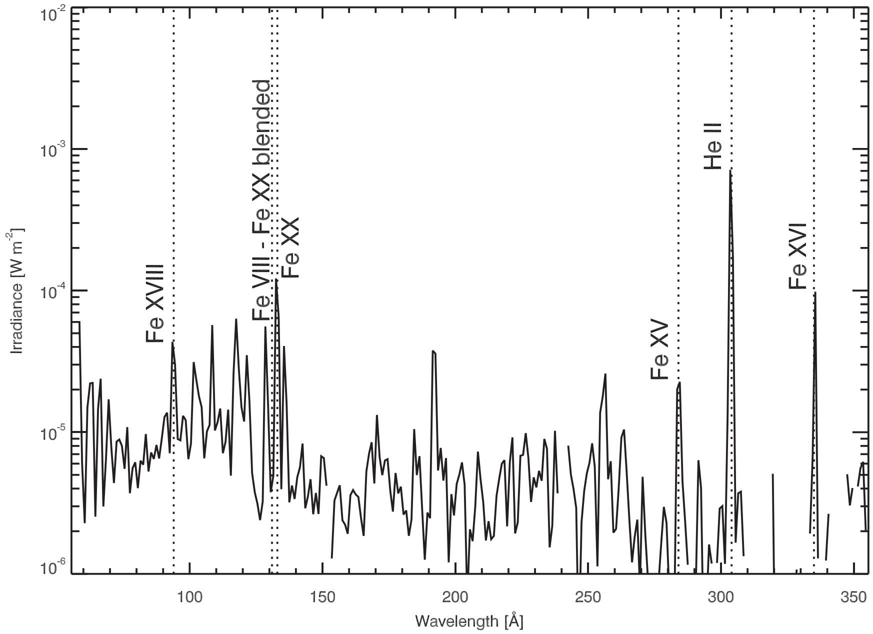

Figure 2. EUV spectrum of the peak time of Fe VIII–Fe XX blended and Fe XX (19:54 UT) for the M6.3-class flare on 2013 November 1 observed by SDO/EVE MEGS-A. This EUV spectrum is subtracted from the preflare background. The EUV flare lines that focused on this study are indicated as the vertical dotted lines.

features. The GOES satellites are a stationary meteorological satellite series, continuously launched since 1975. The GOES X-ray sensor (XRS) was used for observing solar soft X-ray emissions at two wavelength bands in the ranges of 0.5–4 Å (short channel) and 1–8 Å (long channel) (Bornmann et al. 1996). The long channel was used for identification of solar flare occurrence and class. The peak flux, flux time derivative peak, rise time, and decay time of the soft X-ray emissions were considered the fundamental parameters of the solar flares in this study. The peak flux is the maximum value of soft X-ray flux when a flare occurs (=GOES class). For determining rise time and decay time of soft X-ray emissions, the soft X-ray flux time derivative, shown in the lower panel of Figure 1 (black line), were used. We derived a 30 s running average of the soft X-ray flux time derivative (red line in Figure 1) in order to eliminate short time variation. The flare start time is defined as the first time to reach 5% of the flux derivative peak, and the flare end time is defined as the time when the flux time derivative reaches 5% of the flux derivative minus peak. Therefore, the soft X-ray rise time is determined as time from flare start (obtained from the upper method) to peak time, and the decay time is determined as time from flare peak to end time (obtained from the upper method), respectively. Figure 1 shows the parameters obtained by the GOES light curve for the M6.3-class flare on 2013 November 1. The peak flux is 6.3×10^{-5} W m^{-2}, the flux derivative peak is 7.4×10^{-7} W m^{-2} s^{-1}, the rise time is 285 s, and the decay time is 751 s. The standard deviation of the GOES soft X-ray flux was 5.2×10^{-9} W m^{-2} for this event. This is ~0.008% of the flare peak flux, and the standard deviation for all analyzed events was almost the same percentage.

2.2. *EUV Spectrum during the Flare Observed by the SDO/EVE MEGS-A*

The EUV spectrum during the flare observed by the SDO/EVE MEGS-A is shown in Figure 2. This study has focused on six EUV lines observed by MEGS-A, Fe VIII–Fe XX blended 131 Å, Fe XV 284 Å, Fe XVI 335 Å, Fe XVIII 94 Å, Fe XX 133 Å, and He II 304 Å, which were strongly enhanced during solar flare. We used the 1 Å integrated lines in order to eliminate the influence of wavelength shift related to flare Doppler velocity (Hudson 2011), and also inherent instrument design (Chamberlin 2016). Formation temperature for these EUV lines are different; the Fe XX 133 Å originate from the ~9–13 MK plasma (the hottest line), the Fe XVIII 94 Å is from ~6 MK plasma, the Fe XVI 335 Å is from ~3 MK plasma, the Fe XV 284 Å is from ~2 MK plasma, the Fe VIII–Fe XX blended 131 Å is from ~0.4–13 MK plasma, and the He II 304 Å is approximately from the ~0.05 MK plasma (the coolest line). Fe VIII–Fe XX blended 131 Å behaves like a cool corona line during nonflaring times, while it behaves like a hot corona line during flare. Figure 3 shows the light curves for these six lines. An average of 3 minutes of EUV emission flux before the flare start was subtracted from the flare emission as the background. Then, a 110 s running average (dotted light curves in Figure 3) was used to delete the short time variation in EUV emissions. The peak time and flux of EUV line emission are determined from this running-averaged profile. We obtained the EUV emission parameters from EUV light curves for the M6.3-class flare on 2013 November 1 (Figure 3). For flux parameters, the Fe VIII–Fe XX blended peak flux is 2.3×10^{-5} W m^{-2}, the Fe XV peak flux is 1.4×10^{-4} W m^{-2}, the Fe XVI peak flux is 5.2×10^{-4} W m^{-2}, the Fe XVIII peak flux is 2.2×10^{-4} W m^{-2}, the Fe XX peak flux is 6.5×10^{-4} W m^{-2}, and the He II peak flux is 4.2×10^{-3} W m^{-2}. For temporal parameters, the EUV rise time was determined from the soft X-ray flare start time to peak time of EUV emissions in this study. The Fe VIII–Fe XX blended rise time is 332 s, the Fe XV rise time is 432 s, the Fe XVI rise time is 452 s, the Fe XVIII rise time is 422 s, the Fe XX rise time is 312 s, and the He II rise time is 282 s. In this event, the rise time was He II, Fe XX, Fe VIII–Fe XX blended, Fe XVIII, Fe XV, and Fe XVI from the earliest. The standard deviation of EUV emission for Fe VIII–Fe XX blended is 2.0×10^{-6} W m^{-2}, for Fe XV

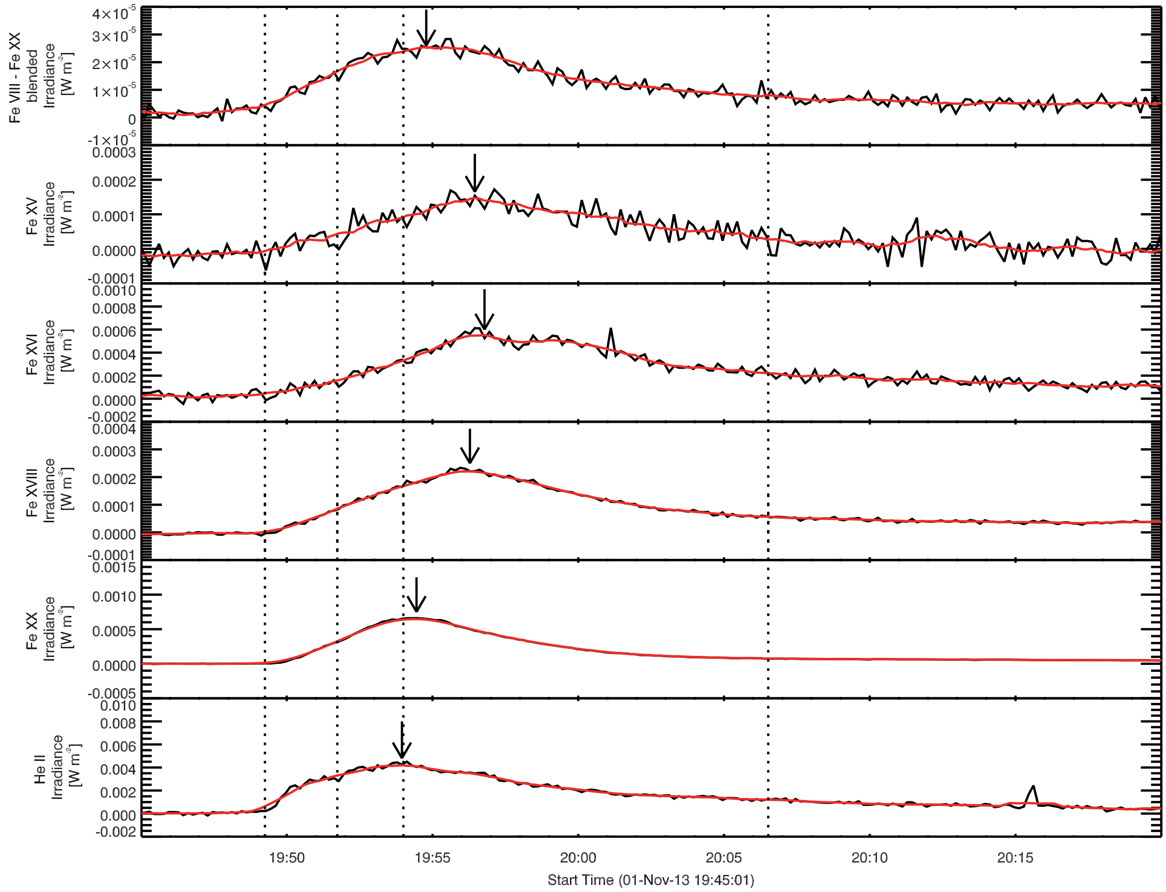

Figure 3. Light curves of EUV line (Fe VIII–Fe XX blended, Fe XV, Fe XVI, Fe XVIII, Fe XX, and He II) emission obtained by SDO/EVE during the M6.3-class flare on 2013 November 1. Solid lines indicate raw observed data with background subtraction, and red lines indicated a 110 s running average of raw data. Each vertical dotted line indicates the soft X-ray start time, derivative peak time, peak time, and end time, respectively, from left to right. Each arrow indicates the peak time for each EUV emission line.

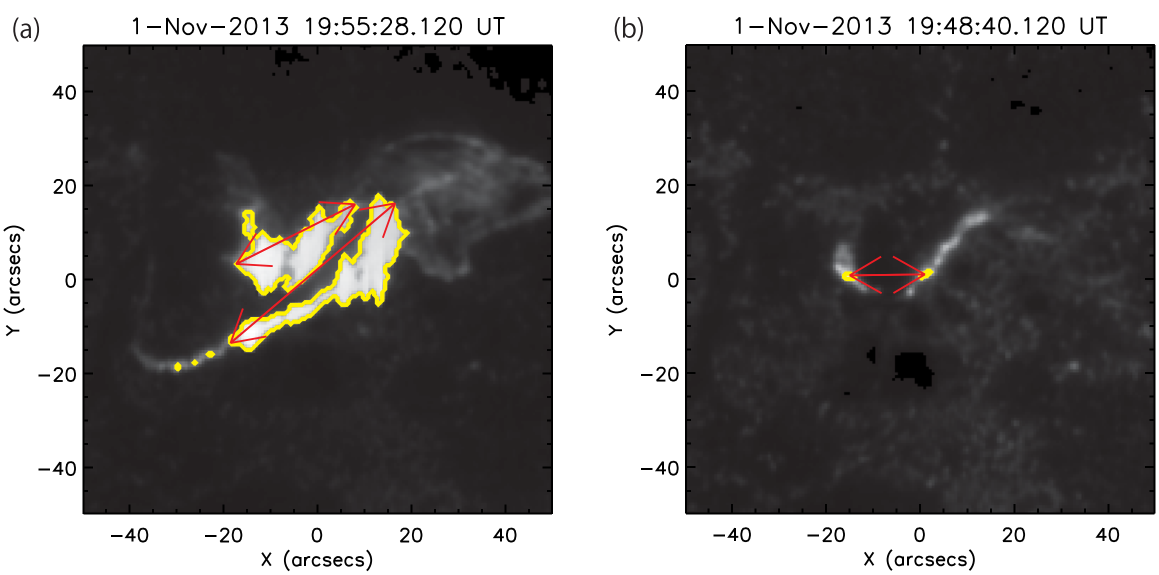

Figure 4. (a) Sample SDO/AIA image for determination of ribbon length. The yellow contour shows 40σ intensity from the background (=ribbon area). The red arrows show ribbon length. (b) Sample SDO/AIA image for determination of ribbon distance. The yellow contour shows 40σ intensity from the background. The ribbon distance is shown by the red arrows.

is 1.3×10^{-5} W m^{-2}, for Fe XVI is 2.6×10^{-5} W m^{-2}, for Fe XVIII is 3.7×10^{-6} W m^{-2}, for Fe XX is 9.4×10^{-7} W m^{-2}, and for He II is 1.0×10^{-4} W m^{-2} in this event, respectively. These are ∼8.5%, ∼9.3%, ∼5.0%, ∼1.6%, ∼0.1%, and ∼2.5% of each EUV line peak flux, respectively. Fe XV has quite a large standard deviation due to the relatively smaller enhancement.

Table 1
Time Evolution Parameters of Flares from GOES and SDO/EVE

Date	GOES	Soft X-Ray Time (UT)				EUV Peak Time (UT)					
yyyy/mm/dd	Class	Start	Derivative Peak	Peak	End	Fe VIII–Fe XX Blended	Fe XV	Fe XVI	Fe XVIII	Fe XX	He II
2010/11/06	M5.4	15:31:07	15:34:56	15:36:45	15:56:06	15:38:06	15:41:16	15:40:46	15:39:26	15:37:16	15:35:06
2011/02/13	M6.6	17:31:50	17:34:14	17:38:01	18:09:50	17:39:12	17:41:42	17:41:12	17:40:12	17:38:32	17:34:52
2011/07/30	M9.3	02:07:08	02:08:22	02:09:30	02:17:27	02:10:05	02:10:55	02:10:55	02:10:25	02:09:55	02:08:45
2011/08/03	M6.0	13:21:11	13:34:34	13:48:07	14:50:20	13:51:16	13:49:46	13:48:56	13:55:46	13:49:06	13:50:46
2011/08/08	M3.5	18:02:48	18:05:53	18:10:37	18:40:33	18:14:37	18:23:57	18:21:27	18:16:57	18:10:57	18:04:47
2011/09/04	M3.2	11:36:24	11:40:11	11:44:56	12:00:24	11:48:53	…	…	11:48:53	11:46:13	11:41:33
2011/09/24	M3.1	17:19:35	17:21:44	17:25:37	17:47:09	17:28:19	…	…	17:30:19	17:26:39	…
2011/09/25	M7.4	04:31:43	04:44:33	04:50:26	…	04:54:29	04:58:49	04:58:29	04:55:39	04:51:19	04:54:29
2011/09/25	M3.7	15:26:46	15:31:12	15:33:13	15:45:12	15:33:09	15:38:39	15:38:59	15:35:29	15:33:49	15:31:59
2011/09/26	M4.0	05:05:51	05:07:13	05:08:16	…	05:09:59	…	05:11:29	05:11:19	05:08:49	05:07:19
2011/10/02	M3.9	00:40:42	00:46:16	00:50:16	1:20:55	00:53:41	00:58:21	00:56:31	00:56:11	00:51:01	00:45:31
2011/11/05	M3.7	02:51:04	03:30:58	03:35:12	05:02:34	03:52:50	04:44:40	04:43:50	03:54:10	03:36:50	03:32:30
2012/01/23	M8.7	03:38:06	03:49:25	03:58:53	06:00:15	04:11:11	04:13:01	04:11:51	04:08:11	03:59:11	03:41:11
2012/01/27	X1.7	18:08:22	18:27:05	18:36:44	19:45:23	18:46:03	18:49:03	18:49:03	18:48:13	18:39:03	18:54:23
2012/03/07	X5.4	00:13:05	00:18:12	00:24:49	01:03:54	00:27:23	00:35:43	00:35:43	00:28:33	00:25:53	00:19:03
2012/03/09	M6.3	03:24:21	03:26:16	03:53:30	…	03:53:44	04:01:54	04:01:44	03:58:54	03:52:34	03:40:24
2012/05/09	M4.7	12:27:22	12:29:49	12:32:05	12:43:29	12:33:11	…	12:36:01	12:34:31	12:32:51	12:31:21
2012/05/09	M4.1	21:01:45	21:03:17	21:05:26	21:17:29	21:06:51	…	21:08:31	21:07:21	21:05:41	21:03:31
2012/06/03	M3.3	17:52:15	17:53:49	17:55:13	18:03:43	17:54:17	17:57:27	17:57:07	17:56:07	17:55:07	17:54:17
2012/07/04	M5.3	09:51:36	09:54:24	09:55:16	10:01:45	09:56:54	…	09:57:44	09:57:14	09:55:44	09:53:24
2012/07/04	M4.6	22:04:45	22:07:10	22:09:34	22:30:45	22:10:14	…	22:14:24	22:12:14	22:09:44	22:07:24
2012/07/05	M4.7	03:34:35	03:35:30	03:36:07	03:40:27	…	03:38:04	03:38:14	03:37:34	03:37:14	03:37:04
2012/07/05	M6.1	11:41:44	11:43:38	11:44:31	11:46:20	11:45:24	11:46:54	11:47:04	11:46:04	11:45:14	11:44:14
2012/07/08	M6.9	16:25:39	16:30:16	16:32:07	17:04:08	16:36:45	…	16:37:55	16:37:15	16:33:25	16:31:05
2012/07/12	X1.4	16:11:23	16:32:51	16:52:47	18:49:33	17:06:55	17:13:35	17:22:45	17:08:55	16:50:25	16:55:35
2012/10/22	M5.0	18:45:27	18:47:14	18:51:48	19:12:41	18:53:41	19:36:51	19:33:31	18:53:41	18:51:41	18:49:41
2012/10/23	X1.8	03:14:36	03:15:48	03:17:22	3:32:13	03:18:01	03:19:11	03:18:31	03:18:31	03:18:01	03:16:11
2012/11/13	M6.0	02:00:59	02:02:29	02:03:59	02:13:08	20:05:37	02:06:07	02:06:17	02:05:37	02:04:57	02:03:17
2013/04/11	M6.5	06:57:21	07:09:12	07:16:36	7:44:09	07:23:46	07:32:46	07:31:36	07:24:46	07:16:26	07:10:26
2013/04/12	M3.3	20:30:20	20:35:49	20:37:58	21:11:09	20:41:47	…	20:41:27	20:40:07	20:38:07	20:36:37
2013/05/14	X3.2	01:02:54	1:08:03	01:11:50	1:40:02	01:13:34	01:15:34	01:15:14	01:14:24	01:12:04	01:15:44
2013/05/15	X1.2	01:29:25	01:42:52	01:48:03	02:21:02	01:53:35	01:54:25	01:53:35	01:52:35	01:49:05	01:54:55
2013/06/07	M5.9	22:33:51	22:43:28	22:49:49	23:44:43	22:54:30	22:47:10	22:53:00	22:54:00	22:51:10	22:45:30
2013/10/24	M3.5	10:30:48	10:32:49	10:33:26	10:48:11	10:33:05	10:34:25	10:34:15	10:34:15	10:33:55	10:32:55
2013/10/26	M3.1	19:23:36	19:25:06	19:27:15	19:41:25	19:28:16	…	19:31:06	19:29:46	19:27:36	19:24:16
2013/10/27	M3.5	12:38:06	12:45:59	12:48:26	13:07:33	12:50:36	…	12:50:56	12:51:16	12:48:56	12:39:36
2013/10/28	M5.1	04:35:36	04:38:52	04:41:24	04:51:04	04:42:26	…	04:46:36	04:44:56	04:42:16	04:39:46
2013/10/28	M4.4	15:06:29	15:10:40	15:15:17	15:29:43	15:17:36	15:24:16	15:23:06	15:19:16	15:15:16	15:11:16
2013/10/29	X2.3	21:45:58	21:50:02	21:54:36	22:17:08	21:56:06	…	22:10:36	21:57:06	21:55:26	22:11:46
2013/11/01	M6.3	19:49:15	19:51:44	19:54:00	20:06:31	19:54:47	19:56:27	19:56:47	19:56:17	19:54:27	19:53:57
2013/11/05	X3.3	22:10:39	22:11:51	22:12:50	22:20:39	22:14:18	22:15:28	22:15:28	22:14:38	22:13:38	22:11:58
2013/11/06	M3.8	13:42:27	13:44:09	13:46:14	13:59:00	13:48:08	13:53:38	13:53:38	13:51:58	13:50:08	13:45:58
2013/11/08	X1.1	04:23:30	04:24:44	04:25:53	04:39:59	04:26:59	04:29:29	04:28:59	04:27:39	04:26:29	04:24:59
2013/11/10	X1.1	05:10:33	05:12:38	05:14:26	05:31:34	05:13:59	05:19:19	05:18:39	05:17:09	05:15:09	05:13:29
2013/11/19	X1.0	10:17:06	10:22:33	10:26:04	10:57:55	10:29:42	10:30:52	10:30:52	10:30:22	10:28:12	10:22:22
2013/12/29	M3.1	07:52:08	07:53:55	07:56:20	08:09:35	07:57:42	…	07:58:12	07:58:12	07:56:22	07:53:42
2014/01/01	M9.9	18:43:07	18:46:51	18:52:08	19:26:53	18:54:53	18:54:33	18:55:03	18:54:33	18:52:13	18:47:03
2014/02/12	M3.7	04:15:28	04:20:54	04:25:10	04:52:26	04:30:44	04:31:34	04:31:04	04:29:24	04:25:34	04:33:14
2014/02/20	M3.0	07:40:02	07:44:14	07:56:00	09:19:17	08:06:16	08:02:56	08:03:16	08:11:26	08:00:46	07:45:26
2014/03/12	M9.3	22:31:22	22:32:44	22:34:21	22:50:56	22:35:31	…	22:36:31	22:36:21	22:35:21	22:32:51

The standard deviation of each EUV line for all analyzed events was almost the same percentage. Note that the He II line often has an earlier peak than the soft X-ray peak, that is, there is peak in the impulsive phase. Furthermore, for the light curve of the He II line, a single peak is often observed due to the mixture of impulsive and gradual phases.

2.3. Geometrical Features of the Flare Observed by the SDO/AIA

For determining the geometrical features of the solar flare, we used UV images observed by SDO/Atmospheric Imaging Assembly (AIA; Lemen et al. 2012). The SDO/AIA observe UV and EUV emissions from the Sun using 10 bands in the

Table 2
Emission Parameters of Flare from GOES and SDO/EVE

Date	Soft X-Ray	GOES	Soft X-Ray Flux		EUV Peak Flux (W m^{-2})					
yyyy/mm/dd	Peak Time (UT)	Class	Peak (W m^{-2})	Derivative Peak (W m^{-2} s^{-1})	Fe VIII–Fe XX Blended	Fe XV	Fe XVI	Fe XVIII	Fe XX	He II
2010/11/06	15:36:45	M5.4	5.4E−05	5.9E−07	1.8E−05	2.4E−04	7.5E−04	1.9E−04	5.1E−04	1.4E−03
2011/02/13	17:38:01	M6.6	6.6E−05	8.6E−07	2.2E−05	1.7E−04	6.2E−04	2.2E−04	6.2E−04	2.6E−03
2011/07/30	02:09:30	M9.3	9.3E−05	2.2E−06	3.2E−05	2.6E−04	8.5E−04	3.3E−04	1.0E−03	3.8E−03
2011/08/03	13:48:07	M6.0	6.0E−05	1.6E−07	2.4E−05	2.8E−04	8.0E−04	2.6E−04	5.4E−04	1.6E−03
2011/08/08	18:10:37	M3.5	3.5E−05	2.5E−07	1.2E−05	1.9E−04	4.2E−04	1.3E−04	2.4E−04	8.3E−04
2011/09/04	11:44:56	M3.2	3.2E−05	2.5E−07	9.6E−06	…	…	7.1E−05	1.2E−04	3.3E−04
2011/09/24	17:25:37	M3.1	3.1E−05	2.1E−07	1.3E−05	…	…	7.1E−05	1.4E−04	…
2011/09/25	04:50:26	M7.4	7.4E−05	2.5E−07	2.6E−05	2.6E−04	7.4E−04	2.6E−04	6.0E−04	2.4E−03
2011/09/25	15:33:13	M3.7	3.7E−05	5.0E−07	2.1E−05	1.5E−04	3.7E−04	1.6E−04	3.0E−04	5.0E−03
2011/09/26	05:08:16	M4.0	4.0E−05	9.2E−07	1.4E−05	…	2.2E−04	1.1E−04	3.3E−04	2.4E−03
2011/10/02	00:50:16	M3.9	3.9E−05	2.6E−07	1.4E−05	1.5E−04	4.1E−04	1.7E−04	4.1E−04	1.6E−03
2011/11/05	03:35:12	M3.7	3.7E−05	6.3E−08	1.8E−05	2.5E−04	6.2E−04	2.2E−04	4.2E−04	7.4E−04
2012/01/23	03:58:53	M8.7	8.7E−05	2.6E−07	3.1E−05	5.1E−04	1.4E−03	4.6E−04	8.0E−04	2.7E−03
2012/01/27	18:36:44	X1.7	1.7E−04	4.5E−07	5.9E−05	5.6E−04	1.9E−03	7.2E−04	1.2E−03	1.8E−03
2012/03/07	00:24:49	X5.4	5.4E−04	2.5E−06	1.2E−04	5.5E−04	1.7E−03	9.0E−04	3.5E−03	8.6E−03
2012/03/09	03:53:30	M6.3	6.3E−05	3.8E−07	2.4E−05	3.8E−04	9.5E−04	3.4E−04	6.5E−04	4.8E−03
2012/05/09	12:32:05	M4.7	4.7E−05	4.6E−07	1.8E−05	…	1.8E−04	1.5E−04	3.9E−04	3.1E−03
2012/05/09	21:05:26	M4.1	4.1E−05	7.4E−07	1.2E−05	…	2.5E−04	1.4E−04	3.8E−04	3.3E−03
2012/06/03	17:55:13	M3.3	3.3E−05	7.5E−07	1.6E−05	1.9E−04	5.6E−04	1.9E−04	3.6E−04	5.1E−03
2012/07/04	09:55:16	M5.3	5.3E−05	7.8E−07	1.4E−05	…	1.7E−04	8.8E−05	3.4E−04	5.6E−03
2012/07/04	22:09:34	M4.6	4.6E−05	6.0E−07	1.6E−05	…	2.8E−04	1.6E−04	4.1E−04	3.2E−03
2012/07/05	03:36:07	M4.7	4.7E−05	1.3E−06	…	1.2E−04	2.2E−04	6.5E−05	1.9E−05	1.8E−03
2012/07/05	11:44:31	M6.1	6.1E−05	1.4E−06	1.8E−05	1.4E−04	2.6E−04	1.1E−04	2.7E−04	8.1E−03
2012/07/08	16:32:07	M6.9	6.9E−05	6.6E−07	2.4E−05	…	3.8E−04	1.5E−04	2.9E−04	2.4E−03
2012/07/12	16:52:47	X1.4	1.4E−04	2.6E−07	4.4E−05	3.6E−04	1.2E−03	4.0E−04	1.2E−03	3.9E−03
2012/10/22	18:51:48	M5.0	5.0E−05	7.1E−07	1.5E−05	1.5E−04	3.7E−04	9.3E−05	3.2E−04	7.9E−04
2012/10/23	03:17:22	X1.8	1.8E−04	4.0E−06	3.4E−05	1.6E−04	3.8E−04	2.0E−04	9.0E−04	3.3E−03
2012/11/13	02:03:59	M6.0	6.0E−05	1.3E−06	1.5E−05	1.8E−04	4.2E−04	1.3E−04	3.3E−04	4.0E−03
2013/04/11	07:16:36	M6.5	6.5E−05	2.4E−07	2.9E−05	4.4E−04	1.2E−03	4.3E−04	7.6E−04	4.7E−03
2013/04/12	20:37:58	M3.3	3.3E−05	2.7E−07	1.1E−05	…	4.2E−04	1.8E−04	3.2E−04	1.1E−03
2013/05/14	01:11:50	X3.2	3.2E−04	2.8E−06	7.5E−05	2.9E−04	8.8E−04	6.0E−04	2.2E−03	2.0E−03
2013/05/15	01:48:03	X1.2	1.2E−04	6.1E−07	4.5E−05	3.8E−04	9.8E−04	4.8E−04	1.0E−03	1.9E−03
2013/06/07	22:49:49	M5.9	5.9E−05	3.0E−07	2.0E−05	1.5E−04	4.2E−04	1.1E−04	3.1E−04	1.4E−03
2013/10/24	10:33:26	M3.5	3.5E−05	6.6E−07	1.7E−05	1.5E−04	5.3E−04	2.0E−04	3.3E−04	3.2E−03
2013/10/26	19:27:15	M3.1	3.1E−05	3.8E−07	9.8E−06	…	3.0E−04	1.1E−04	2.3E−04	9.6E−04
2013/10/27	12:48:26	M3.5	3.5E−05	3.1E−07	1.2E−05	…	3.9E−04	1.3E−04	2.9E−04	1.2E−03
2013/10/28	04:41:24	M5.1	5.1E−05	5.6E−07	1.9E−05	…	2.7E−04	1.3E−04	2.5E−04	3.3E−03
2013/10/28	15:15:17	M4.4	4.4E−05	2.3E−07	2.0E−05	3.0E−04	8.3E−04	2.4E−04	4.6E−04	4.3E−03
2013/10/29	21:54:36	X2.3	2.3E−04	1.6E−06	3.8E−05	…	1.6E−04	2.4E−04	1.0E−03	6.5E−04
2013/11/01	19:54:00	M6.3	6.3E−05	7.4E−07	2.3E−05	1.4E−04	5.2E−04	2.2E−04	6.5E−04	4.2E−03
2013/11/05	22:12:50	X3.3	3.3E−04	9.5E−06	5.1E−05	2.5E−04	7.9E−04	3.6E−04	1.8E−03	5.6E−03
2013/11/06	13:46:14	M3.8	3.8E−05	6.5E−07	1.7E−05	1.1E−04	2.7E−04	1.2E−04	3.2E−04	3.7E−03
2013/11/08	04:25:53	X1.1	1.1E−04	2.9E−06	3.1E−05	1.6E−04	5.4E−04	2.6E−04	9.9E−04	7.6E−03
2013/11/10	05:14:26	X1.1	1.1E−04	2.1E−06	3.8E−05	1.5E−04	7.6E−04	3.1E−04	9.6E−04	1.0E−02
2013/11/19	10:26:04	X1.0	1.0E−04	8.9E−07	3.1E−05	1.5E−04	5.2E−04	1.9E−04	4.1E−04	9.7E−04
2013/12/29	07:56:20	M3.1	3.1E−05	4.2E−07	1.7E−05	…	2.4E−04	1.4E−04	3.6E−04	2.4E−03
2014/01/01	18:52:08	M9.9	9.9E−05	8.1E−07	3.7E−05	2.0E−04	6.9E−04	3.0E−04	6.6E−04	6.2E−03
2014/02/12	04:25:10	M3.7	3.7E−05	2.0E−07	1.6E−05	2.0E−04	6.8E−04	2.2E−04	3.8E−04	1.6E−03
2014/02/20	07:56:00	M3.0	3.0E−05	1.3E−07	1.3E−05	1.5E−05	4.5E−04	1.1E−04	1.8E−04	9.5E−04
2014/03/12	22:34:21	M9.3	9.3E−05	1.8E−06	2.2E−05	…	2.4E−04	1.3E−04	3.2E−04	5.4E−04

range of 94–4500 Å. The spatial resolution is $1\farcs5$, and the time resolution is 12 s. We focused on the flare ribbon region because the flare ribbon strongly associates with the flare loop that is source of soft X-ray and EUV emissions. We extracted the ribbon distance and length as parameters in order to investigate the flare ribbon in detail. Figures 4(a) and (b) show the SDO/AIA 1600 Å image used for the determination of ribbon length and distance. Flare ribbon regions with intensities of 40σ higher than the background were chosen. These are shown as contours in Figures 4(a) and (b). We defined the flare ribbons that have the two largest independent areas surrounded by contours as mentioned above. Before extracting the parameters, the locations of all flare ribbons were moved closer to the solar center using solar software

Table 3
Geometrical Parameters of Flares from SDO/AIA

Date	Soft X-Ray	GOES	Location on Disk (arcsec)		1600 Å Ribbon (arcsec)	
yyyy/mm/dd	Peak Time (UT)	Class	Longitude	Latitude	Distance	Length
2010/11/06	15:36:45	M5.4	−909	−187	…	93.1
2011/02/13	17:38:01	M6.6	−894	−135	10.1	…
2011/07/30	02:09:30	M9.3	−532	164	14.0	…
2011/08/03	13:48:07	M6.0	554	−223	69.5	76.5
2011/08/08	18:10:37	M3.5	806	212	…	113.4
2011/09/04	11:44:56	M3.2	897	288	…	…
2011/09/24	17:25:37	M3.1	−760	157	18.5	24.8
2011/09/25	04:50:26	M7.4	839	342	67.4	…
2011/09/25	15:33:13	M3.7	−651	134	32.7	…
2011/09/26	05:08:16	M4.0	−527	124	10.4	30.4
2011/10/02	00:50:16	M3.9	230	63	30.7	33.7
2011/11/05	03:35:12	M3.7	−663	301	94.3	…
2012/01/23	03:58:53	M8.7	−954	−207	86.6	65.4
2012/01/27	18:36:44	X1.7	833	551	…	…
2012/03/07	00:24:49	X5.4	−485	397	26.2	…
2012/03/09	03:53:30	M6.3	−743	232	66.7	53.1
2012/05/09	12:32:05	M4.7	−483	260	12.7	30.7
2012/05/09	21:05:26	M4.1	−419	256	14.8	29.0
2012/06/03	17:55:13	M3.3	−567	275	5.9	29.6
2012/07/04	09:55:16	M5.3	−912	255	8.9	30.0
2012/07/04	22:09:34	M4.6	431	−316	17.5	37.8
2012/07/05	03:36:07	M4.7	439	−343	3.6	23.9
2012/07/05	11:44:31	M6.1	−954	251	8.5	36.7
2012/07/08	16:32:07	M6.9	908	−280	…	…
2012/07/12	16:52:47	X1.4	62	−294	…	155.2
2012/10/22	18:51:48	M5.0	−770	259	…	67.4
2012/10/23	03:17:22	X1.8	−805	−266	…	…
2012/11/13	02:03:59	M6.0	55	380	8.2	…
2013/04/11	07:16:36	M6.5	726	−306	33.1	…
2013/04/12	20:37:58	M3.3	599	411	29.0	83.8
2013/05/14	01:11:50	X3.2	−918	147	…	196.6
2013/05/15	01:48:03	X1.2	−867	192	…	105.8
2013/06/07	22:49:49	M5.9	−24	−273	…	…
2013/10/24	10:33:26	M3.5	207	33	13.9	…
2013/10/26	19:27:15	M3.1	−942	−206	…	…
2013/10/27	12:48:26	M3.5	−908	−218	…	…
2013/10/28	04:41:24	M5.1	909	113	…	52.9
2013/10/28	15:15:17	M4.4	−457	−176	22.4	…
2013/10/29	21:54:36	X2.3	972	85	…	…
2013/11/01	19:54:00	M6.3	−775	123	15.6	53.8
2013/11/05	22:12:50	X3.3	−661	−257	22.0	26.9
2013/11/06	13:46:14	M3.8	−545	−265	12.4	36.9
2013/11/08	04:25:53	X1.1	−225	−278	20.0	67.6
2013/11/10	05:14:26	X1.1	227	−280	6.5	41.2
2013/11/19	10:26:04	X1.0	884	−247	…	83.5
2013/12/29	07:56:20	M3.1	23	−232	18.6	33.4
2014/01/01	18:52:08	M9.9	671	−240	23.3	59.0
2014/02/12	04:25:10	M3.7	−8	−116	21.0	…
2014/02/20	07:56:00	M3.0	905	−237	…	50.5
2014/03/12	22:34:21	M9.3	908	269	…	…

drot_map.pro.[5] Ribbon length was defined as the length of both ends of each the largest ribbon regions, and we extracted the total of two ribbon lengths around the flare end time, indicated by arrows in Figure 4(a). Ribbon distance was defined as the distance between two points having the highest brightness in two ribbons just before the flare start time, which is indicated by the red arrow in Figure 4(b). For the M6.3-class flare on 2013 November 1, the ribbon distance and length are estimated to be 15″.6 and 53″.8, respectively.

3. Statistical Analysis to Find Effective Parameters for Flare Emissions

The events observed by SDO/EVE, which had been observing solar flare EUV spectra with sufficient temporal

[5] https://hesperia.gsfc.nasa.gov/ssw/gen/idl/maps/drot_map.pro

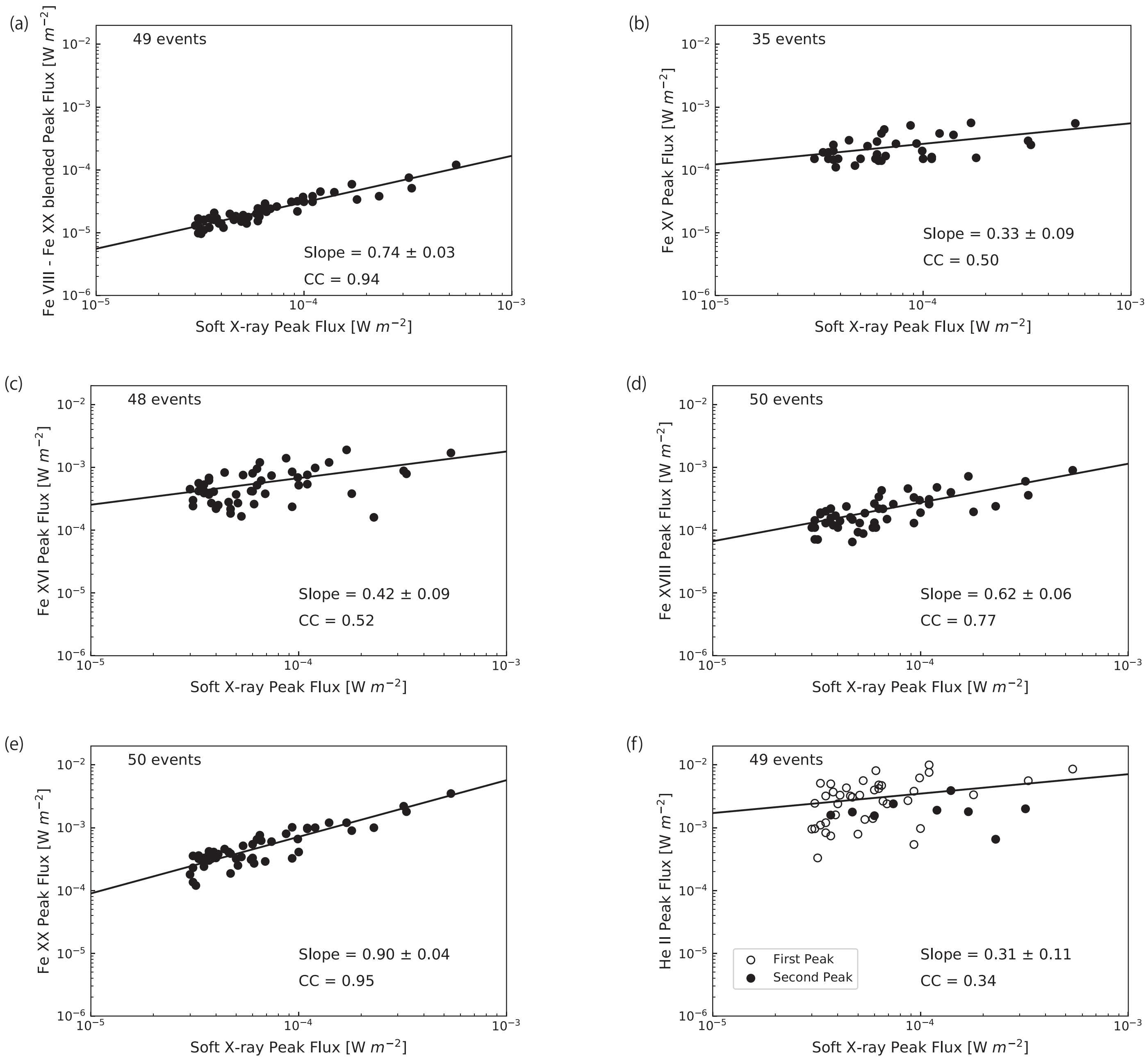

Figure 5. Relationship between soft X-ray peak flux and EUV line peak flux of Fe VIII–Fe XX blended (a), Fe XV (b), Fe XVI (c), Fe XVIII (d), Fe XX (e), and He II (f). For He II (f), the outlined and filled dots indicate the first peak earlier than the soft X-ray peak time and the second peak later than the soft X-ray peak time, respectively.

and spectral resolution, were selected as analysis events for this statistical research. First, we selected events larger than the M3-class flare that occurred between 2010 November and 2014 May from the Hinode flare catalog (Watanabe et al. 2012). Within this selected time period and flare class, there were 50 flare events observed by the SDO/EVE MEGS-A. As the fundamental parameters, the start, peak, and end times of soft X-rays are shown in Table 1, and the soft X-ray peak flux and flux derivative peak are shown in Table 2. For EUV emission data, only flare events with a clear peak flux of 5 times larger than the standard deviation of preflare background were used. The Fe XVIII and Fe XX lines satisfied the above criteria in all 50 events, the Fe VIII–Fe XX blended and He II lines in 49 events, the Fe XVI line in 48 events, and the Fe XV line in 35 events. Since He II has two peaks in both the impulsive phase and the gradual phase, we defined the peak earlier than GOES peak time as the He II first peak, and the peak later than GOES peak time as the He II second peak. In this study, there were 40 events with the first peak of He II and 9 events with the second peak. The value of peak time and peak flux of each EUV line are shown in Tables 1 and 2, respectively. For the geometrical features of the flare, flare ribbons are clearly observed at the 1600 Å band in SDO/AIA for 32 events. In particular, limb flare events have large geometrical uncertainties, so disk flare and limb flare events were distinguished by a threshold of 600″ from the center of the solar disk. In this study, there were 19 disk flares and 13 limb flares. The ribbon distance and length of these events are shown in Table 3.

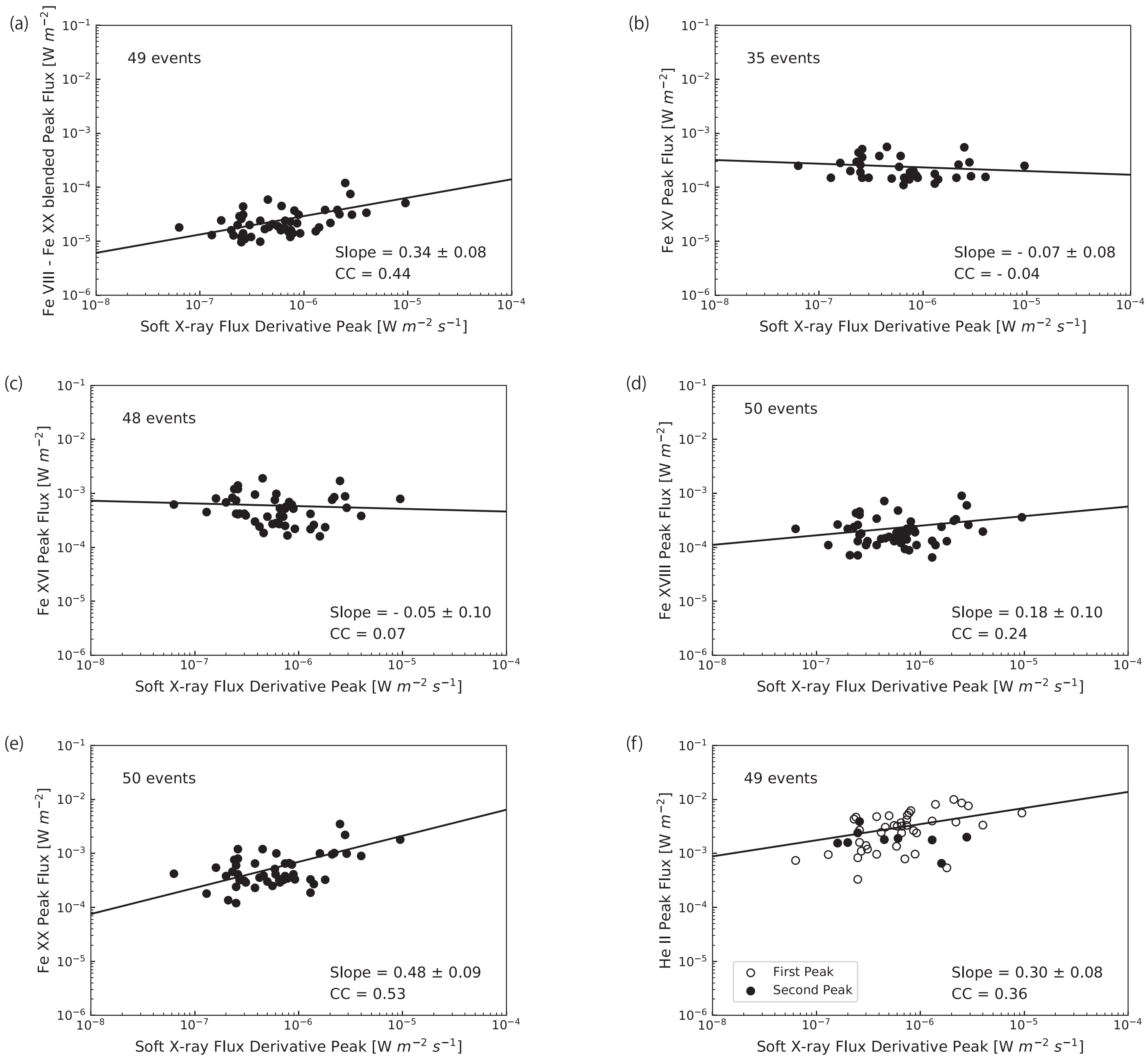

Figure 6. Relationship between the soft X-ray flux derivative peak and EUV line peak flux of Fe VIII–Fe XX blended (a), Fe XV (b), Fe XVI (c), Fe XVIII (d), Fe XX (e), and He II (f). For He II (f), the outlined and filled dots indicate the first peak earlier than the soft X-ray peak time and the second peak later than the soft X-ray peak time, respectively.

3.1. Statistical Analysis for EUV Emissions with SDO/EVE

Using the EUV data and flare fundamental parameters obtained in Section 2.1, statistical analysis was performed to evaluate the relationships of these emissions. The relationships between EUV peak flux and soft X-ray peak flux were first evaluated. The Fe VIII–Fe XX blended and Fe XX showed strong correlation, with correlation coefficients of 0.94 (Figure 5(a)) and 0.95 (Figure 5(e)), respectively. The Fe XVIII have moderate correlation, with a correlation coefficient of 0.77 (Figure 5(d)). However, Fe XV and Fe XVI showed weaker correlation than other Fe lines, with correlation coefficients of 0.50 (Figure 5(b)) and 0.52 (Figure 5(c)), respectively. The He II also showed the weakest correlation, with a correlation coefficient of 0.34 (Figure 5(f)).

The relationships between the EUV peak flux and soft X-ray flux derivative peak were also evaluated. Fe VIII–Fe XX blended and Fe XX showed weak correlation, with correlation coefficients of 0.44 (Figure 6(a)) and 0.53 (Figure 6(e)), respectively. He II also showed weak correlation, with a correlation coefficient 0.36 (Figure 6(f)). Meanwhile, Fe XV, Fe XVI, and Fe XVIII have no correlation with the soft X-ray flux derivative peak (Figures 6(b)–(d).)

The time evolution of EUV lines was then evaluated and compared with soft X-ray rise time. All EUV lines have strong correlation with the soft X-ray rise time (Figure 7). When the regression line is above the straight line with a slope of 1, the EUV line has a longer rise time than the soft X-ray rise time. When the slope is larger than 1, the EUV line has a longer rise

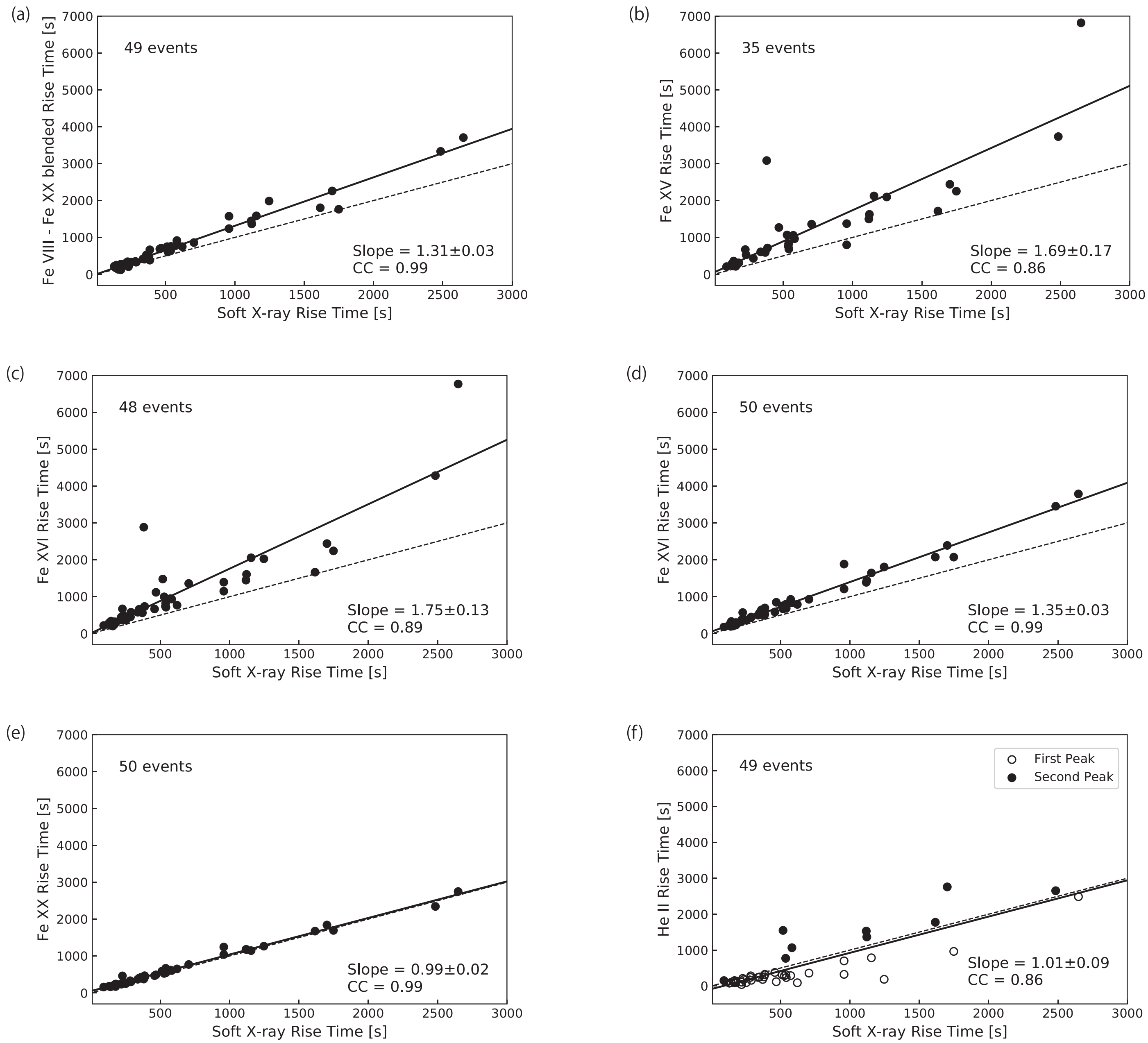

Figure 7. Relationship between the soft X-ray rise time and EUV line rise time of Fe VIII–Fe XX blended (a), Fe XV (b), Fe XVI (c), Fe XVIII (d), Fe XX (e), and He II (f). In each panel, the dashed line indicates the straight line with a slope of 1. For He II (f), the outlined and filled dots indicate the first peak earlier than the soft X-ray peak time and the second peak later than the soft X-ray peak time, respectively.

time than the soft X-ray rise time. In the opposite case, the rise time of the EUV line is shorter than the soft X-ray rise time. From the slopes shown in Figure 7, the Fe XX (the hottest line) and He II lines exhibited shorter rise times among these EUV lines. Subsequently, the Fe VIII–Fe XX blended and Fe XVIII and, finally, the Fe XV and Fe XVI lines rise almost simultaneously.

3.2. Statistical Analysis for Flare Geometrical Features with SDO/AIA

We evaluated the relationship between flare geometrical features and the flare fundamental parameters as shown in Figure 8. The relation of the ribbon distance and the soft X-ray rise and decay time showed strong correlation, with correlation coefficients of 0.92 (Figure 8(a)) and 0.91 (Figure 8(b)), respectively. On the other hand, the relation of the ribbon length and the soft X-ray rise and decay time showed weak correlation, with correlation coefficients of 0.50 (Figure 8(c)) and 0.43 (Figure 8(d)), respectively. As shown in Figure 8, the analyzed events were classified into disk flare (white circle) and limb flare (black dot) with a threshold of 600″ from the solar disk center. There is no significant difference due to the flare locations in the scatterplots. Therefore, the effect of flare location is considered to be smaller than expected when using the parameter described in Section 2.3.

4. Discussion and Summary

Statistical analysis of flare emission observed by SDO/EVE and AIA was conducted to have a better understanding of the flare EUV spectra and profile. The flare fundamental

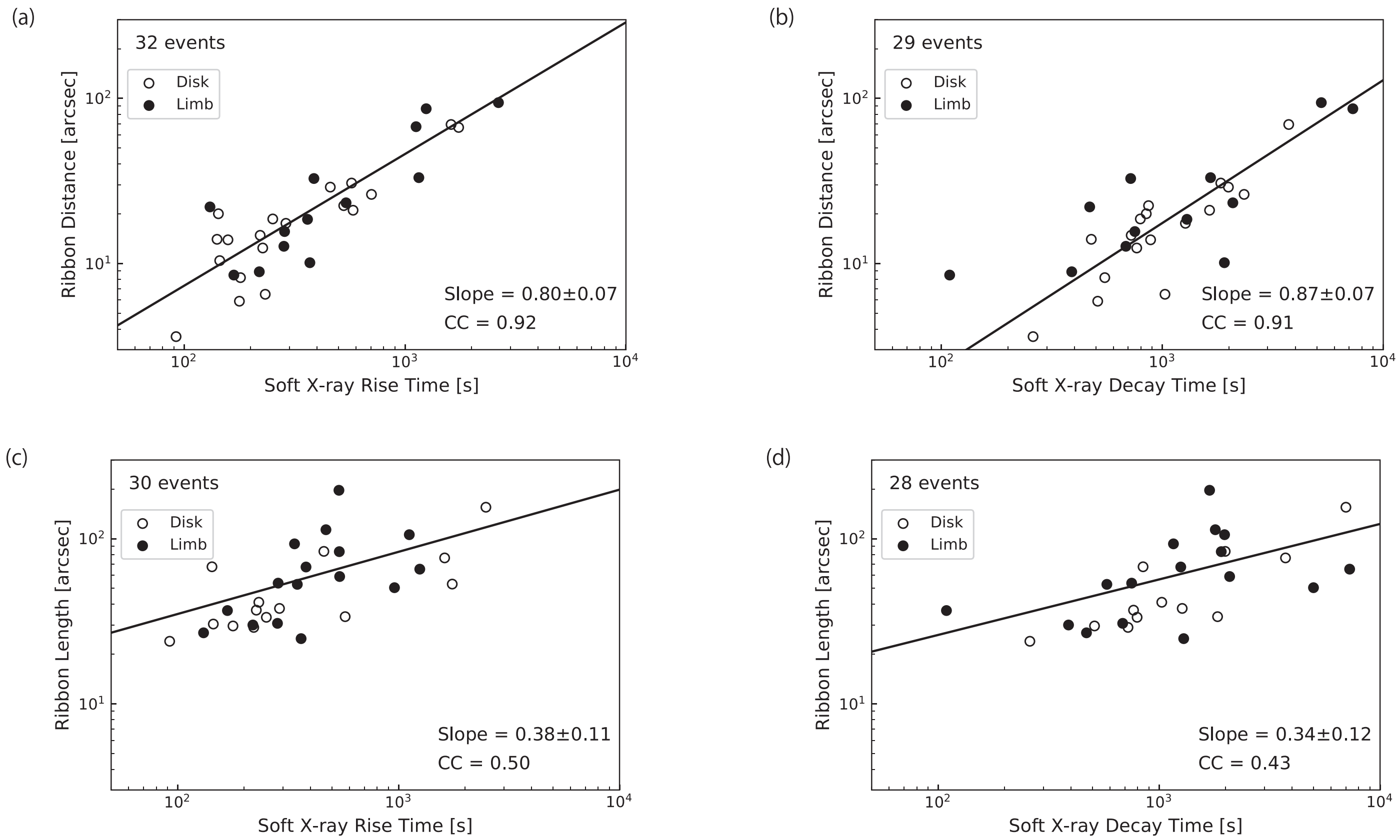

Figure 8. (a) Relationship between the ribbon distance and the soft X-ray rise time. (b) Relationship between the ribbon distance and the soft X-ray decay time. (c) Relationship between the ribbon length and the soft X-ray rise time. (d) Relationship between the ribbon length and the soft X-ray decay time. Each outlined and filled point indicates the flare that occurred within and outside 600″ from the solar disk center, respectively.

parameters obtained from GOES soft X-ray data were compared with EUV line peak flux, rise and decay time, and geometrical features.

Regarding the peak flux correlation between the EUV line and soft X-ray, the hotter Fe lines (Fe VIII–Fe XX blended 131 Å ∼ 0.4–13 MK and Fe XX 133 Å ∼ 9−13 MK) have strong correlation (Figures 5(a) and (e)), and Fe XVIII 94 Å ∼ 6 MK (Figure 5(d)) have moderate correlation with the soft X-ray peak flux. However, the cooler Fe lines (Fe XV 284 Å ∼ 2 MK and Fe XVI 335 Å ∼ 3 MK) have weak correlation (Figures 5(b) and (c)). In particular, as shown by the analyzed number of events, we can see the weak enhancement on the Fe XV line. This result indicates that the relatively longer wavelength EUV lines, Fe XV and Fe XVI, emitted from relatively cooler plasmas are not proportional to the soft X-ray flux.

Regarding the relationship between the EUV peak flux and the soft X-ray flux derivative peak, the hotter Fe lines (Fe VIII–Fe XX blended and Fe XX) have weak correlation with the soft X-ray flux derivative peak (Figures 6(a) and (e)). On the other hand, the cooler Fe lines (Fe XV and Fe XVI) have no correlation with the flux derivative peak (Figures 6(b) and (c)). According to the Neupert effect (Neupert 1968), the soft X-ray flux time derivative roughly represents the impulsive phase. Therefore, this result indicates that Fe line emissions along with the initial heating of the coronal loop may be related to the impulsive phase.

In regard to the correlation of rise time, regardless of the strength of the flux and the flux correlation, all Fe lines have strong correlation with the soft X-ray (Figures 7(a)–(e)). Previous studies have observed peak time differences in the EUV line and reported that the hot line peaks earlier than the cold line (Woods et al. 2011; Cheng et al. 2019), and this is considered to be because these EUV lines are originated from the cooling of the flaring loop. According to the statistical examination, this aspect was obscured for Fe lines (Figures 7(a)–(e)). The hottest Fe XX emitted from ∼9 to 13 MK plasma has the shortest rise time. Subsequently, Fe VIII–Fe XX blended emitted from ∼0.4 to 13 MK plasma, and Fe XVIII emitted from the ∼6 MK plasma, and finally Fe XVI emitted from ∼3 MK and Fe XV emitted from ∼2 MK plasma lines peaked almost simultaneously. This is presumably due to the blending of multiple emission lines in these EUV lines at 1 Å resolution.

He II 304 Å line peak flux has weak correlation with the soft X-ray peak flux (Figure 5(f)) and has the shortest rise time (Figure 7(f)). It is known that the He II line emission is from the transition region (Woods et al. 2011). Thus, the He II line emission is considered to be in a nonthermal emission, so we applied the Neupert effect and compared it with the soft X-ray flux derivative peak. However, the correlation between the He II line peak flux and the soft X-ray flux derivative peak is weak (Figure 6(f)), so it cannot be clearly determined as nonthermal emission. At least, from the above results, it was found that it is difficult to estimate the He II line flux from thermal emission such as soft X-rays.

When regarding the correlation of the geometrical features of the flare, the flare ribbon distance showed strong correlation with both the rise time and decay time of soft X-ray flux, respectively. The rise time is the duration from the start of flare to the time when evaporated plasma fills the loop. The decay time is the time required for the filled plasma in the flare loop to cool down, and is considered to be related not only to the depth of the flare loop but also to the overall volume of the flare loop. The ribbon distance is considered to be correlated with the loop length of the flare. So it is considered that the time evolution of flare emission is mostly determined by the loop length. Furthermore, from the viewpoint of the standard model of flare, the loop length affects the radiative cooling rate of the coronal loop, which can affect the difference from the EUV emission temperature.

As described above, this study attempted to determine the physical parameters that affect the flare emission spectra by summarizing the statistical characteristics of flare emissions. The hotter Fe line emissions showed strong correlation with soft X-ray flux in many cases. However, our statistical study revealed that the EUV flare peak flux of the Fe XV, Fe XVI, and He II lines have weak correlation with the soft X-ray peak flux. Our results indicated that the time evolution of the EUV line emission during solar flares may or may not be related to soft X-rays. Accordingly, it seems that empirical models using GOES data may not be able to accurately reproduce the these line emissions during flare. Therefore, in order to accurately reproduce the emission of each EUV line, it is important to physically describe the distribution of temperature and density of the emitting plasma in the flare loop and foot-points.

We first would like to thank the referee for meaningful comments and suggestions that improved this paper. The authors would like to thank K. Ichimoto, T. Kawai, S. Takasao, H. Jin, S. Toriumi, H. P. Warren, and J. W. Reep for stimulating and fruitful discussions. Part of this work was conducted by the joint research program of the Institute for Space-Earth Environmental Research (ISEE), Nagoya University. This study was supported by JSPS KAKENHI grant Nos. JP15H05816, JP16H01187, and JP18H04452.

ORCID iDs

Kyoko Watanabe https://orcid.org/0000-0003-0321-7881
Shinsuke Imada https://orcid.org/0000-0001-7891-3916
Tomoko Kawate https://orcid.org/0000-0002-1021-0322
Kyoung-Sun Lee https://orcid.org/0000-0002-4329-9546

References

Bornmann, P. L., Speich, D., Hirman, J., et al. 1996, Proc. SPIE, 2812, 291
Cargill, P. J., Bradshaw, S. J., & Klimchuk, J. A. 2012, ApJ, 785, 5
Cargill, P. J., Mariska, J. T., & Antiochos, S. P. 1995, ApJ, 439, 1034
Carmichael, H. 1964, NASSP, 50, 451
Chamberlin, P. C. 2016, SoPh, 291, 1665
Chamberlin, P. C., Woods, T. N., & Eparvier, F. G. 2007, SpWea, 5, S07005
Chamberlin, P. C., Woods, T. N., & Eparvier, F. G. 2008, SpWea, 6, S05001
Cheng, Z., Wang, Y., Liu, R., Zhou, Z., & Liu, K. 2019, ApJ, 875, 93
Dellinger, J. H. 1937, JAP, 8, 732
Donnelly, R. F. 1976, JGR, 81, 4745
Hirayama, T. 1974, SoPh, 34, 323
Hudson, H. S. 2011, SSRv, 158, 5
Imada, S., Aoki, K., Hara, H., et al. 2013, ApJL, 776, L11
Imada, S., Murakami, I., & Watanabe, T. 2015, PhPl, 22, 101206
Innes, D. E., McKenzie, D. E., & Wang, T. J. 2003, SoPh, 217, 267
Jachhia, L. 1990, Natur, 183, 526
Judge, D. L., McMullin, D. R., Ogawa, H. S., et al. 1998, SoPh, 177, 161
Kane, S. R. 1974, in IAU Symp. 57, Coronal Disturbances, ed. G. A. Newkirk (Dordrecht: Reidel), 105
Klimchuk, J. A., Patsourakos, S., & Cargill, P. J. 2008, ApJ, 682, 1351
Kopp, R. A., & Pneuman, G. W. 1976, SoPh, 50, 85
Lee, K.-S., Imada, S., Watanabe, K., Bamba, Y., & Brooks, D. H. 2017, ApJ, 836, 150
Lemen, J. R., Title, A. M., Boerner, P. F., et al. 2012, SoPh, 275, 17
Milligan, R. O., & Dennis, B. R. 2009, ApJ, 699, 968
Neupert, W. N. 1968, ApJL, 153, L59
Qian, L., Burns, A. G., Chamberlin, P. C., & Solomon, S. C. 2010, JGRA, 115, 09311
Qian, L., Burns, A. G., Chamberlin, P. C., & Solomon, S. C. 2011, JGRA, 116, 10309
Serio, S., Reale, F., Jakimiec, J., Sylwester, B., & Sylwester, J. 1991, A&A, 241, 197
Shiota, D., Isobe, H., Chen, P. F., et al. 2005, ApJ, 634, 663
Sturrock, P. A. 1966, Natur, 211, 695
Suess, K., Snow, M., Viereck, R., & Machol, J. 2016, SWSC, 6, A10
Thiemann, E. M. B., Eparvier, F. G., Woodraska, D., et al. 2019, SWSC, 9, A43
Thiemann, E. M. B., Eparvier, F. G., & Woods, T. N. 2017, SWSC, 7, A36
Toriumi, T., Schrijver, C., Harra, L., Hudson, H., & Nagashima, K. 2017, ApJ, 834, 56
Warren, H. P., Brooks, D. H., Ugarte-Urra, I., et al. 2018, ApJ, 854, 122
Watanabe, K., Masuda, S., & Segawa, T. 2012, SoPh, 279, 317
Woods, T. N., Eparvier, F. G., Bailey, S. M., et al. 2005, JGRA, 110, A01312
Woods, T. N., Eparvier, F. G., Hock, R., et al. 2012, SoPh, 275, 115
Woods, T. N., Hock, R., Eparvier, F. G., et al. 2011, ApJ, 739, 59
Yokoyama, T., & Shibata, K. 1998, ApJL, 494, L113